Atomic Structure Amorphization and Electronic Structure Reconstruction of $FeCoNiCrMo_x$ High-Entropy Alloy Nanoparticles for Highly Efficient Water Oxidation

Xuechun Zhou, He Zhu, Shu Fu, Si Lan, Horst Hahn, Jianrong Zeng, and Tao Feng**

The complexity of the multielement interaction in high-entropy alloys (HEAs) may provide more active sites to adapt different catalytic reaction steps in oxygen evolution reaction (OER). Investigating the correlation between structure and performance of HEAs electrocatalysts is both essential and challenging. In this work, $FeCoNiCrMo_x$ HEA nanoparticles are successfully fabricated utilizing a unique nanofabrication method called inert gas condensation. With the increase of high-valence metal component Mo, the atomic structure amorphization and electronic structure reconstruction are unveiled. According to the X-ray photoelectron spectroscopy valence spectra, the d-band center of $FeCoNiCrMo_x$ is ascending, and thus enhancing the adsorption energy. Synchrotron pair distribution function analysis reflects the degree of structural disorder and reveals a robust correlation with the intrinsic OER activities of the electrocatalysts. $FeCoNiCrMo_{1.0}$ high-entropy metallic glass nanoparticles exhibit an outstanding OER performance with an ultralow overpotential of 294.5 mV at a high current density of 100 mA cm^{-2}. This work brings fundamental and practical insights into the modulation mechanism of metal components of HEAs catalysts for developing OER.

1. Introduction

A critical juncture has been reached with regard to the demand for sustainable and clean energy sources.[1] It's a daunting and monumental challenge as the world grapples, with growing energy scarcity. Alkaline water electrolysis to hydrogen technology commercialization model has matured, and hydrogen evolution reactions can even reach a very low overpotential in the latest research.[2] However, the high overpotential of the anodic oxygen evolution reaction (OER) is relatively challenging to fall, and the sluggish kinetics involving the transfer of four electrons jeopardizes the overall electrolytic efficiency.[3] Currently, extensive researches have been devoted to exploring non-precious metal catalysts in view of low-cost.[1,3a–c,4] Tailoring the binding energy by alloying can optimize catalytic activity through the induced electronic interactions.[5] As an important factor affecting the catalytic performance, the bonding interactions should neither be strong nor weak.[6] Therefore, high-entropy alloys (HEAs) have been set apart from most of the electrocatalysts owing to their own unique properties.[7]

Considering the further development of HEAs as highly efficient electrocatalysts, the positive multielemental synergy may endow HEAs with enhanced OER properties.[8] Typically, the complex structure of HEAs can be adjusted by flexibly controlling the constituent multielement and their proportions with atomic-level mixing.[9] High entropy effect and "Cocktail effect" may provide multiple active sites, promoting the adsorption and dissociation of oxygen on the surface.[10] The structure–performance relationship behind "cocktail effect" remains largely explored. HEAs possess sluggish diffusion and high formation energy, which contribute to maintaining stability and structural homogeneity.[11] It effectively inhibits the migration and aggregation of metal atoms, delaying electrode deactivation processes and enhancing catalytic lifespan. Meanwhile, the electronic structure of HEAs can be optimized through the lattice distortion effect, which may shift the d-band center and alter the adsorption energy for high catalytic activity.[12] The position of the d-band center based on the d-band model plays a crucial role in the regulation of the adsorption energies and activation energy barriers.[13] The addition of high-valence of transition metal elements (e.g., Cr, Mo, W, Nb, and Ta) is facilitated to the readier oxidation transition to regulate the adsorption energy of *O and *OH and then reduce overpotential.[14] In addition, more

X. Zhou, H. Zhu, S. Fu, S. Lan, T. Feng
Herbert Gleiter Institute of Nanoscience
School of Material Science and Engineering
Nanjing Nanjing University of Science and Technology
Nanjing 210094, P. R. China
E-mail: lansi@njust.edu.cn; tao.feng@njust.edu.cn
H. Hahn
Institute of Nanotechnology
Karlsruhe Institute of Technology
76021 Karlsruhe, Germany
J. Zeng
Shanghai Synchrotron Radiation Facility
Shanghai Advanced Research Institute
Chinese Academy of Sciences
Shanghai 201204, P. R. China
J. Zeng
Shanghai Institute of Applied Physics
Chinese Academy of Sciences
Shanghai 201800, P. R. China

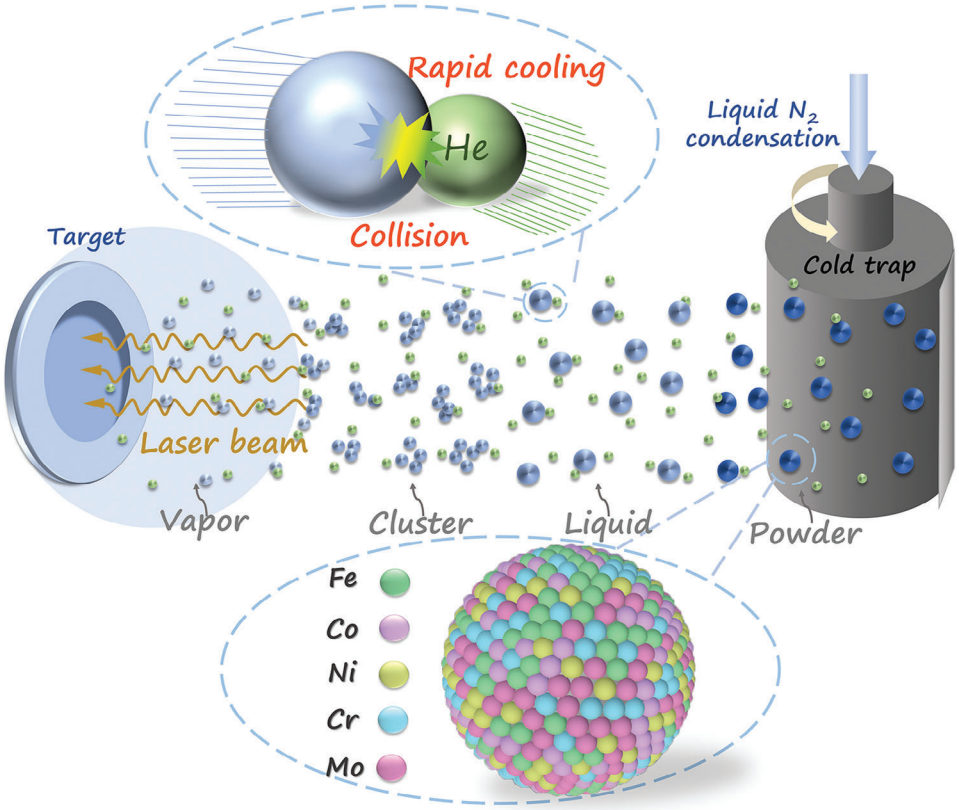

Figure 1. Schematic illustration of the preparation of HEMG-NPs via LE-IGC.

unoccupied d-orbitals can be provided, thus modulating the electronic structure and the electron density of the active site, as well as enhancing the interaction with the reaction mediator. Interestingly, introducing Cr element can even induce a disordered lattice structure, contributing to the formation of amorphous phase,[15] which may further enhance the catalytic activity due to the higher surface energy of amorphous materials than their crystalline counterparts.[16] Therefore, anticipatory rational structural design of catalysts and modulation of their electronic structure predictably are crucial for the development of highly active OER catalysts.

Here, a HEA nanofabrication strategy was proposed via inert gas condensation (IGC) with laser source in picoseconds. In this work, $FeCoNiCrMo_{1.0}$ HEA nanoparticles (NPs) with amorphous structure were successfully achieved by introducing the high-valence metal Mo for the first time. The "cocktail effect" can be taken the maximum advantage by changing the content of Mo element in the HEAs, and $FeCoNiCrMo_{1.0}$ exhibited the best OER catalytic performance with an ultralow overpotential of 294 mV at 100 mA cm^{-2} compared to $FeCoNiCrMo_{0.6}$ and $FeCoNiCrMo_{0.2}$. The randomicity in coordination environment in an amorphous structure leads to the diversification of surface active sites, which is conducive to different catalytic reaction steps. As high-valence metal elements, Mo atoms prefer to be surrounded by lighter atoms of Cr in Mo-rich samples,[17] and the electrons near the Cr atom are more easily attracted to the larger electronegativity of Mo. Indeed, electronegativity and ionization energy are equally important for electron transfer in catalytic processes in view of our pre-work,[18] as well as the Mo (2.16) element possesses electronegativity close to that of noble metal Ru (2.20) and Ir (2.20) element. The optimal electronic structure in HEA NPs can be obtained by adjusting various neighboring atoms and generating an interfacial charge transfer effect. Furthermore, the binding energy of an active site can be governed by the interaction with neighboring atoms.[19] X-ray photoelectron spectroscopy (XPS) valence spectra affirmed that the upshift of the d-band center with the increase of Mo element, plays a vital role in the adsorption of intermediates. Synchrotron pair distribution function (PDF) employed to investigate the impact of short- to medium-range atomic structure on electrocatalytic property. Guidance for the screening of HEA catalysts is provided to explore the correlation between structure and performance.

2. Results and Discussion

2.1. Structure and Morphology Characterization

The high-entropy metallic glass nanoparticles (HEMG-NPs) of $FeCoNiCrMo_{1.0}$ were synthesized by the laser-evaporated inert-gas condensation (LE-IGC) strategy (**Figure 1**). Once the metal atoms are evaporated from the target driven by the focused picosecond pulse laser, and form clusters after initial atomic collisions, then small liquid metal particles rapidly condense to

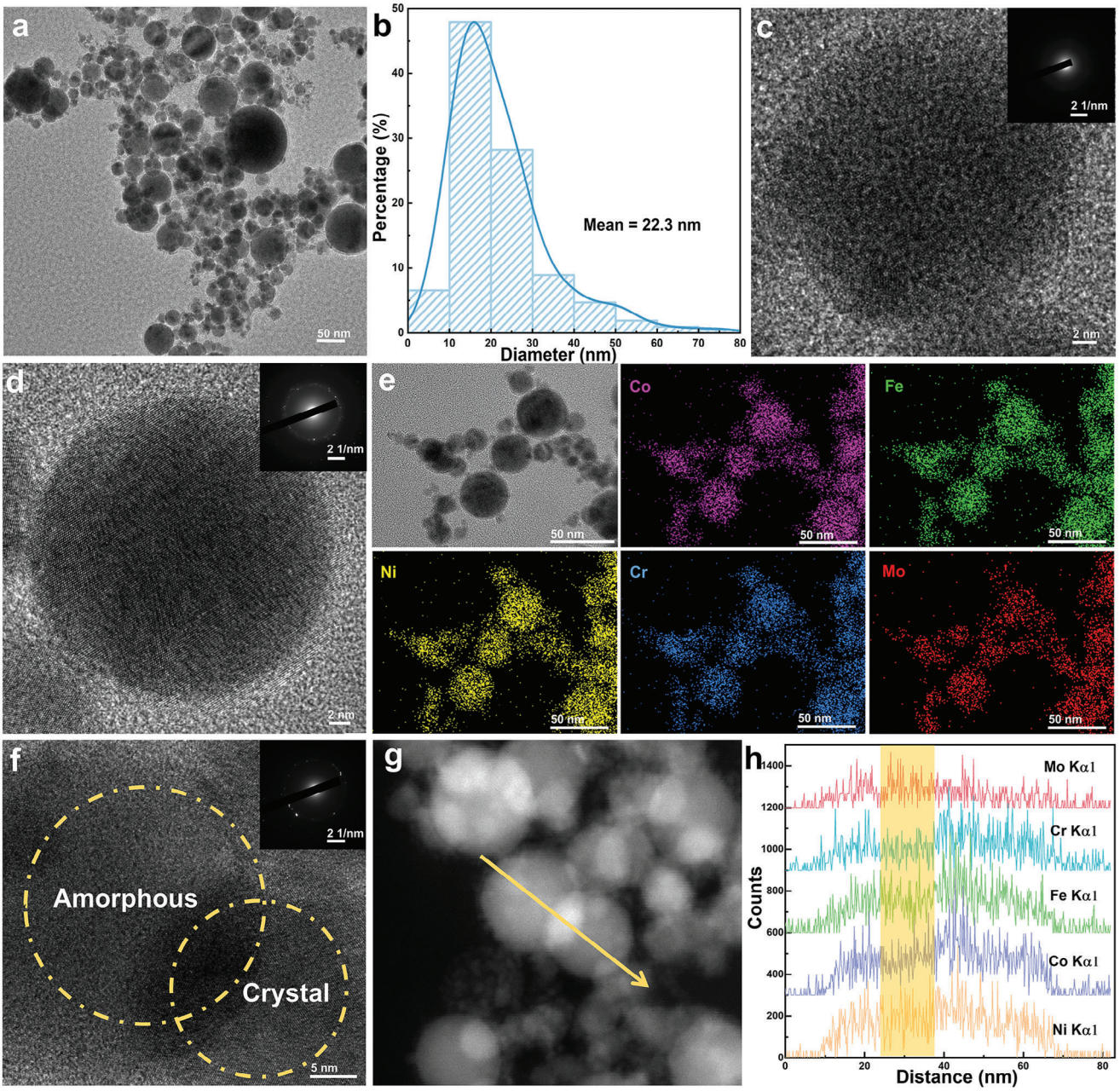

Figure 2. a) TEM of the $FeCoNiCrMo_{1.0}$ NPs sample; b) the corresponding of particle size distribution chart. c) HRTEM and SAED images of the $FeCoNiCrMo_{1.0}$ and d) $FeCoNiCrMo_{0.6}$ NPs. e) TEM and EDS mappings of the $FeCoNiCrMo_{1.0}$ NPs; f) HRTEM and SAED images of g) corresponding HAADF-STEM image taken from the $FeCoNiCrMo_{0.6}$ NPs. h) Compositional profile within the HEA grain highlighted in (g) marked with the yellow line.

form the HEMG-NPs. The unique way of synthesizing HEMG-NPs benefits from the high cooling rate which originates from the collision with gas atoms (Helium), as well as the extremely large temperature gap between vapor region and the liquid-nitrogen-filled cold finger. LE-IGC strategy based on fast cooling at the atomic level, might suppress the precipitation of crystalline phases and form high-entropy solid solutions.[11] It is worth noting that FeCoNiCrMo systems prepared by traditional methods generally form FCC structure,[14,20] rather than the amorphous phase in this work.

As shown in **Figure** 2a,b, a spherical morphology for $FeCoNiCrMo_{1.0}$ with an average size of ≈22.3 nm could be observed. A frequent collision between the FeCoNiCrMo vapor and gas atoms for an accelerated cooling process suppresses the growth of the particles and thus ensure the formation of NPs.[21] The energy dispersive spectroscopy (EDS) mappings and atomic percentages were shown in Figure 2e, Figure S2 and Table S1 (Supporting Information). It is obvious that the constituent elements are homogenously distributed in $FeCoNiCrMo_x$, demonstrating the successful synthesis of $FeCoNiCrMo_x$ HEA NPs.

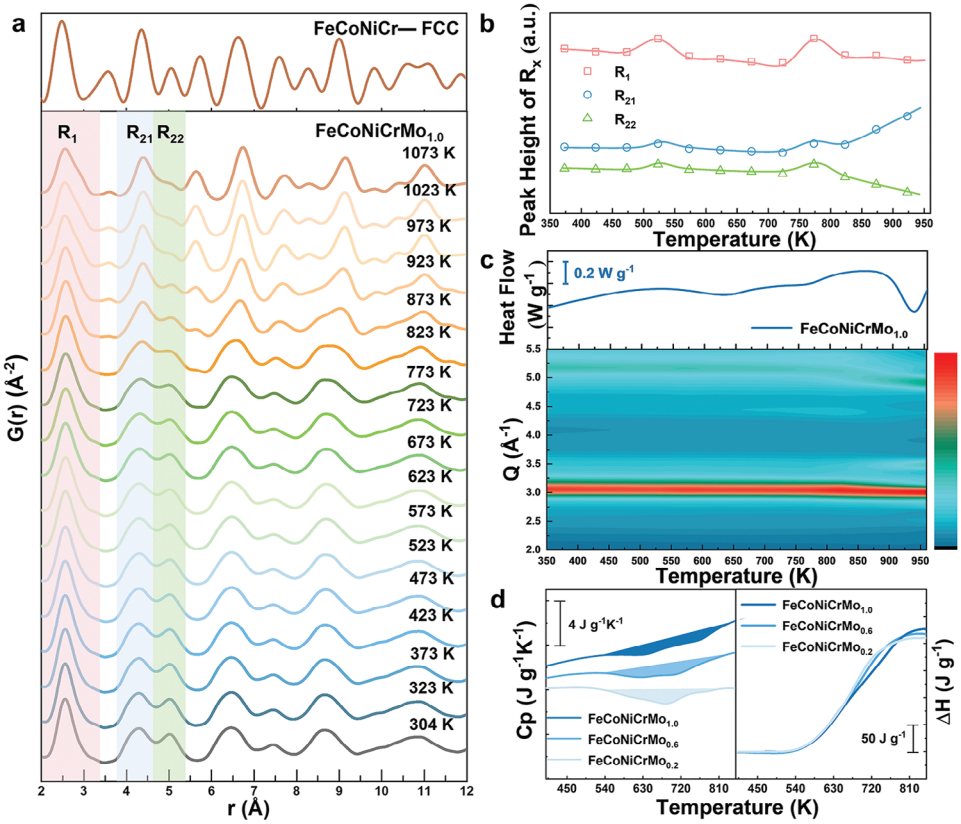

Figure 3. a) In situ high-energy synchrotron X-ray study of $FeCoNiCrMo_{1.0}$ upon heating. b) Peak height of the first coordination shell R_1 and shoulder of the second coordination shell R_{21} and R_{22} as functions of temperature; c) DSC curves of $FeCoNiCrMo_{1.0}$ on the top; The 2D mapping profile of the $S(Q)$ patterns at different temperature for $FeCoNiCrMo_{1.0}$. d) Heat capacity curves of $FeCoNiCrMo_x$ are exhibited on the right for the heating rate of 20 K min^{-1}. Enthalpy change (ΔH) curves obtained by the integration of the heat capacity curves are displayed on the left.

In addition, the effect of Mo content on the phase structure was investigated systematically. From the XRD pattern (Figure S1a, Supporting Information), $FeCoNiCrMo_{0.2}$ showed clear crystallization while a typical broad wind for amorphous structure was observed in $FeCoNiCrMo_{1.0}$. The broad and weak diffraction peaks for $FeCoNiCrMo_{0.6}$ indicate the structure tends to be amorphous but still partially crystallized. The structure changes of the $FeCoNiCrMo_x$ with increasing Mo content were further analyzed in the X-ray structure factor S(Q) (Figure S1b, Supporting Information), and the similar phenomena were also observed which was consistent with the TEM data. The high-resolution transmission electron microscope (HRTEM) image (Figure 2c) showed no lattice fringes on the $FeCoNiCrMo_{1.0}$ particles. Instead, the selected area electron diffraction (SAED) pattern (Figure 2d) showed polycrystalline diffraction rings of $FeCoNiCrMo_{0.2}$. As an intermediate control, the lattice fringe-like patterns (the upper left circle) and typically maze-like amorphous atomic structure (the lower right circle) were both clearly observed in $FeCoNiCrMo_{0.6}$ (Figure 2f). The corresponding SAED image of $FeCoNiCrMo_{0.6}$ showed the broad diffraction rings and several diffraction spots, indicating that it is mostly amorphous and partially crystallized.

To further explore the causes of amorphous formation, the EDS of line sweeps on $FeCoNiCrMo_{0.6}$ from amorphous to crystalline NPs was carried out (Figure 2g). It is evident in Figure 2h that the content of Mo element is from more to less. The increase of Mo exacerbates the lattice distortion and even leads to the transformation of ordered atomic arrangements into disordered ones due to its larger atomic radius than other elements. Atomic size-induced mismatch entropy is vital for the glass-forming ability of amorphous systems. According to the lattice distortion effect in HEA, when the atomic arrangement is unable to maintain the critical point of the lattice array, the lattice array is destroyed and an amorphous structure is formed. The in situ heating synchrotron total scattering was conducted to further explore the thermal stability of FeCoNiCrMo1.0. **Figure 3a** shows the reduced pair distribution function (PDF) $G(r)$ obtained by the Fourier transform of $Q(S(Q)^{-1})$ (Figure S3a, Supporting Information). The first peak R_1 in $G(r)$, corresponding to the nearest-neighbor shell, identifies the structural information of solute-centered short-range order (SRO, 2–5 Å). The shoulder R_2 of the second peak indicates the packing connectivity of SRO on a medium-range scale (5–20 Å). A heat absorption peak can be seen at about 523 K in Figure 3c, and in Figure S3b (Supporting Information), the unusual variation trend occurs for the peak height of Q_1, which transforms from the structure factor $S(Q)$, indicating that the structure tends to be more ordered and corresponding to enthalpy relaxation.[22] Figure 3b shows the peak height of $FeCoNiCrMo_{1.0}$ for R_1, R_{21}, and R_{22}, which all exhibited similar trends of change before 823 K. Analogously, the integrated

intensity for R_1 (integrated region of $G(r) \geq 0$, ≈2.29–2.92 Å) can be seen in Figure S3c (Supporting Information), which slightly increased at about 623 K while a significant increase occurred at about 773 K, matched well with the result of differential scanning calorimetry (DSC). The anomalous exothermic peak can exist in the amorphous,[23] expressing as locally ordered regions and then reentering the disordered state at higher temperatures. It is indicated that the as-prepared sample experiences a glass-to-glass transition from a high-energy state to a low-energy state with a large energy reduction. The presence of a glass-to-glass transition is also a characteristic of high-energy state metallic glass.[24] As the temperature increased, the metastable phase was gradually stabilized, eventually showing an FCC structure similar to FeCoNiCr.[25] Figure 3c is the corresponding 2D mapping profile for the structure factor $S(Q)$ and a distinct crystallization was observed after 823 K. Furthermore, heat capacity measurements were made via DSC at a heating rate of 20 K min^{-1} as shown in Figure 3d (left). The exothermic peaks moved to higher temperatures as the Mo content increased, indicating that $FeCoNiCrMo_{1.0}$ has better thermal stability. To compare the energy state of $FeCoNiCrMo_x$, the enthalpy change (ΔH) curves are plotted as shown in Figure 3d (right) obtained by integrating the heat capacity curves. The ΔH (from 540 to 810 K) of $FeCoNiCrMo_{1.0}$ is the largest, further demonstrating its high energy state. It is worthy to emphasize that amorphous materials with high ΔH value tend to have large free volumes,[26] which makes the surfaces more easily adjustable to accommodate the shapes and sizes of adsorbate molecules, thus enhancing adsorption.

2.2. Structural Performance Correlation

An anodic OER of water splitting was conducted to evaluate the electrocatalytic performance of the FeCoNi, FeCoNiCr, and $FeCoNiCrMo_x$ NPs prepared by LE-IGC. The linear sweep voltammetry (LSV) measurements, as a vital indicator in the assessment, were conducted in an O_2-saturated 1.0 M KOH solution at room temperature. As shown in **Figure** 4a, the conformational entropy of catalytic which obtained via the same preparation method seems to exert a remarkable effect on OER performance. Based on the FeCoNi system, a definite improvement in OER performance occurred with the addition of high-valence Cr and Mo elements, especially for Mo. In addition, the increase of Mo promotes the formation of the amorphous phase, which positively affects catalytic performance. Actually, $FeCoNiCrMo_{1.0}$ HEMG-NPs exhibited the best OER performance among these catalysts, while the commercial RuO_2 showed significantly poor overpotential at a current density of 10 mA cm^{-2} (269.8 mV). The corresponding statistical plots of overpotentials at different current densities are shown more visually in Figure 4b. The $FeCoNiCrMo_{1.0}$ catalyst exhibits the lowest overpotential of 243.3 mV at a current density of 10 mA cm^{-2} and an ultralow overpotential of 294.5 mV at a high current density of 100 mA cm^{-2}. The OER performance trend of $FeCoNiCrMo_{1.0}$ HEMG-NPs at high currents density indicates its great potential for practical application. The catalytic performance of $FeCoNiCrMo_{0.6}$ is only slightly inferior to that of $FeCoNiCrMo_{1.0}$ and much better than that of $FeCoNiCrMo_{0.2}$. This phenomenon corresponds precisely to its structural change, namely, $FeCoNiCrMo_{0.2}$ is clearly crystalline, and $FeCoNiCrMo_{1.0}$ has the best amorphous formation capacity, which is slightly better than that of $FeCoNiCrMo_{0.6}$. It is demonstrated that the high atomic disorder of the system is favorable for catalytic performance. This is also attributed to the unique catalytic activity of HEAs, which emerges from the complex interaction among different elements in a single-phase solid solution. It can be seen that the carbon cloth as the control group had almost no electrochemical activity in Figure S4 (Supporting Information), which proved it only functions as a supporter and current collector during the electrochemical test. Apart from the overpotential, the Tafel slope is another important performance parameter and reflects the energy conversion efficiency of the catalyst. From Figure S5a (Supporting Information), the Tafel slope of $FeCoNiCrMo_{1.0}$, $FeCoNiCrMo_{0.6}$, $FeCoNiCrMo_{0.2}$, FeCoNiCr, FeCoNi, and RuO_2 derived from the LSV curve, are 36.9, 50.8, 65.1, 83.5, 104.8, and 109.3 mV dec^{-1}, respectively. The smallest Tafel slope of $FeCoNiCrMo_{1.0}$ indicated that the determining step was at the end of the multi-electron transfer reaction, which is usually a sign of a good catalyst. The faster kinetics and catalytic rate can be more favorable adsorbing OH^- to form surface intermediate during the OER process. Although the Tafel slope of RuO_2 is larger in our work, it is within a reasonable range as reported in previous literatures.[27] Moreover, the electrochemical activity-specific surface areas (ECSA) of catalysts were investigated by the double-layer capacitance (C_{dl}), which is measured by CV curves (Figure S6, Supporting Information) at various scan rates (10–100 mV s^{-1}) in the non-Faraday region.[28] As illustrated in Figure S5b (Supporting Information), the C_{dl} values of $FeCoNiCrMo_{1.0}$, $FeCoNiCrMo_{0.6}$, $FeCoNiCrMo_{0.2}$, FeCoNiCr, FeCoNi, and RuO_2 were calculated to be 35.96, 35.45, 27.6, 25.84, 14.52, and 23.96 mF cm^2, respectively. The phenomenon indicated that $FeCoNiCrMo_{1.0}$ had a larger electrochemically active area and a higher intrinsic OER activity, which was consistent with the actual electrochemical properties. As an important property for assessing an outstanding catalyst, the catalytic stability was also investigated by chronopotentiometry measurement with a current density of 10, 50, and then 100 mA cm^{-2}. The excellent stability performance of $FeCoNiCrMo_{1.0}$ can be seen in Figure S7 (Supporting Information) for 166 h in 1.0 M KOH. The overpotential is slightly elevated at the beginning, which may be due to the oxidation of the surface that increases the internal resistance or the O_2 bubbles that block up some of the active sites. The EDS mapping of the used $FeCoNiCrMo_{1.0}$ further revealed that the composition of each element is negligibly changed and evenly distributed, and remaining amorphous (Figure S8, Supporting Information), which provided dispersed active sites. The atomic arrangement of HEAs in the amorphous state is disordered and there are no defects such as grain boundaries, segregation, etc., which is conducive to the improvement of corrosion resistance. The high configurational entropy of HEAs decreases the Gibbs free energy of the system and maintains the stability of the internal structure of the alloy.[29] Meanwhile, the OER performance of $FeCoNiCrMo_{1.0}$ in the initial state and after annealing at 973 K for 1 min were compared in Figure 4c. As can be seen in Figure S9a (Supporting Information), the annealed $FeCoNiCrMo_{1.0}$ and $FeCoNiCrMo_{0.6}$ exhibited the same distinct FCC structure as FeCoNiCr. The similar results were observed in Figure 3, in fact, $FeCoNiCrMo_{1.0}$ has begun to crystallize

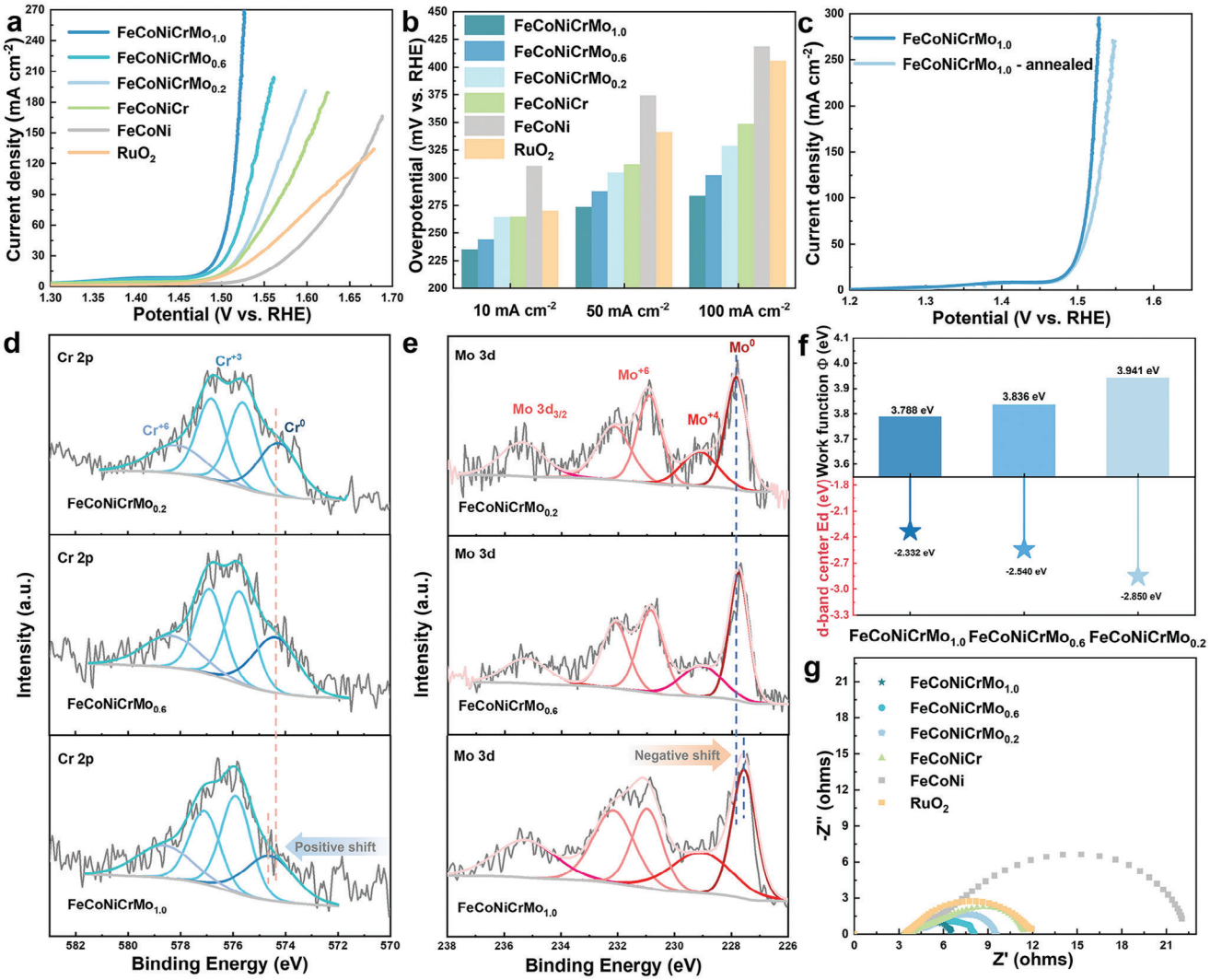

Figure 4. a) IR-corrected polarization curves of the different electrocatalysts for OER in 1.0 M KOH solution at room temperature; b) The overpotential of different electrocatalysts for OER; c) IR-corrected polarization curves of $FeCoNiCrMo_{1.0}$ and $FeCoNiCrMo_{1.0}$ – annealed for OER in 1.0 M KOH solution at room temperature; High-resolution XPS spectra of d) Cr 2p, e) Mo 3d. f) The work functions and d-band centers of $FeCoNiCrMo_{0.2}$, $FeCoNiCrMo_{0.6}$, and $FeCoNiCrMo_{1.0}$. g) The corresponding EIS spectra.

after 823 K. It was obvious that the OER performance was reduced after crystallization, which was in line with the phenomenon observed on $FeCoNiCrMo_{0.6}$ (Figure S9b, Supporting Information), directly demonstrating the advantage of amorphization in the HEA for OER activity.

The electrochemical activity of catalysts is dominated by the electronic structure, and it is essential to analyze the surface electrochemical states of $FeCoNiCrMo_x$ using high-resolution XPS to further reveal the structure–function correlation. As the Cr 2p and Mo 3d spectrum of $FeCoNiCrMo_x$ are displayed in Figure 4d,e. It is noteworthy that the obvious shift to higher binding energy was observed in Cr 2p spectra for $FeCoNiCrMo_{1.0}$ in comparison with that of $FeCoNiCrMo_{0.2}$. In contrast, Mo 3d peaks for $FeCoNiCrMo_{1.0}$ shifted to lower binding energy, manifesting the increased electronic density of Mo after amorphization. Similarly, the electrons near the Cr atom are more easily attracted to the larger electronegativity of Mo (2.16) due to the smaller electronegativity of Cr (1.66) compared with that of Ni (1.91), Co (1.88), and Fe (1.8). Meanwhile, Cr atoms possess the smallest ionization energy (6.7665 eV) compared to those elements, which reflects the very easiness of Cr atomic losing electrons. The interaction between Mo and Cr may facilitate to electron transfer during OER, owing to the electron-donating processes of OER. Therefore, Cr atoms are more favorable for delivering electrons to Mo atoms. The conductivity of the $FeCoNiCrMo_x$ followed an order of $FeCoNiCrMo_{1.0}$ > $FeCoNiCrMo_{0.6}$ > $FeCoNiCrMo_{0.2}$, which was also in line with their catalytic activities in the OER. Moreover, the valence band spectrums (VBS) of $FeCoNiCrMo_x$ were analyzed to obtain the work functions[30] and d-band centers of the samples in Figure 4f (refer to the Experimental Section). $FeCoNiCrMo_{1.0}$ possessed the smallest work function (3.788 eV) compared to $FeCoNiCrMo_{0.6}$ (3.836 eV) and $FeCoNiCrMo_{0.2}$ (3.941 eV). This result represented the lower energy barrier to excite an electron to the vacuum level and escape from the solid

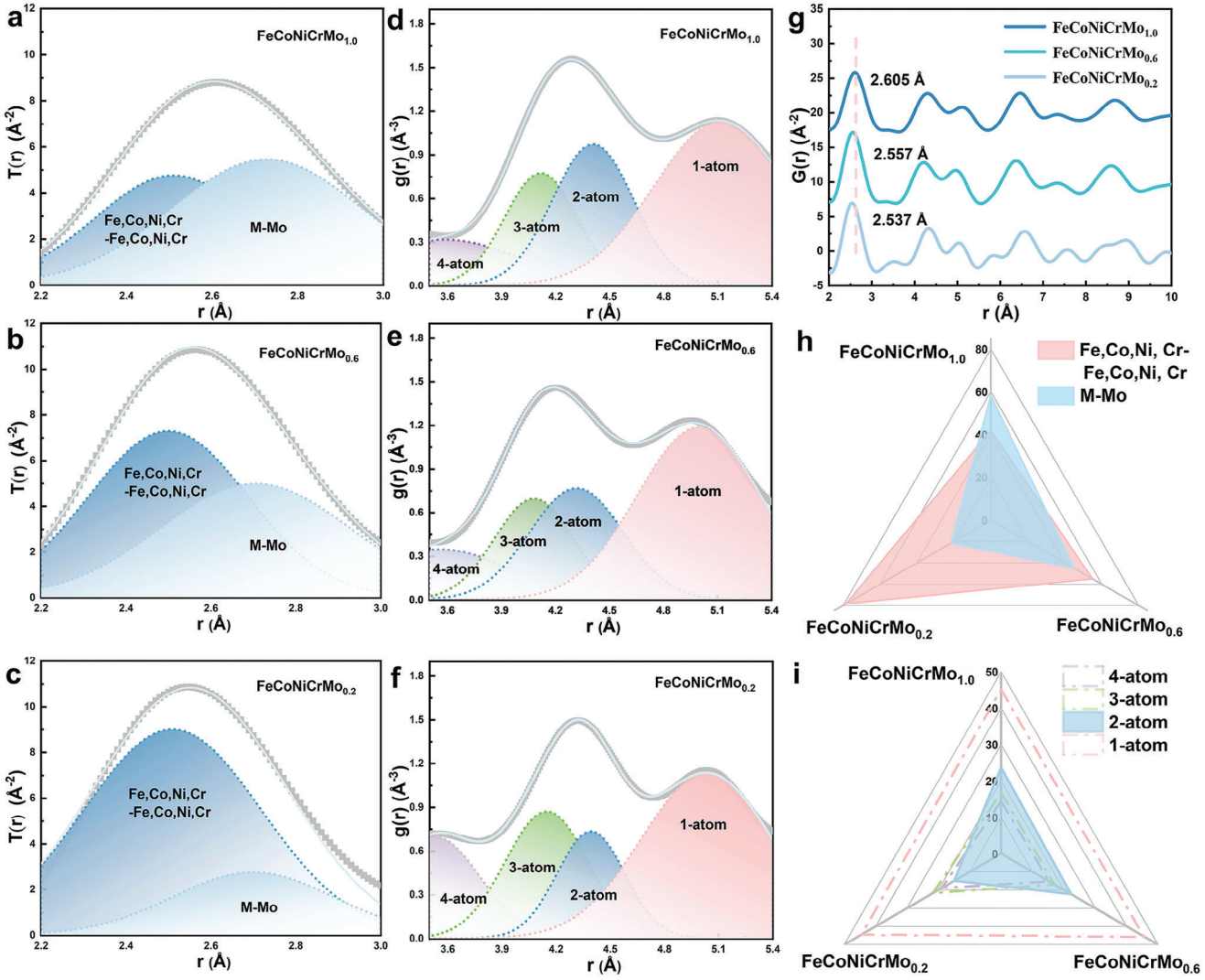

Figure 5. Synchrotron X-ray PDF study of $FeCoNiCrMo_{0.2}$, $FeCoNiCrMo_{0.6}$, and $FeCoNiCrMo_{1.0}$. The fitted results of the first peak $T(r)$s for a) $FeCoNiCrMo_{1.0}$, b) $FeCoNiCrMo_{0.6}$, and c) $FeCoNiCrMo_{0.2}$. The Gaussian fitting results of the second coordination shell in the $g(r)$s for d) $FeCoNiCrMo_{1.0}$, e) $FeCoNiCrMo_{0.6}$, and f) $FeCoNiCrMo_{0.2}$. g) The reduced pair distribution function $G(r)$ patterns. h) The corresponding proportion to the total integrated are of the first coordination shell. i) The corresponding proportion to the total integrated are of the second coordination shell.

surface. As shown in Figure S10 (Supporting Information), with the increase in Mo atomic ratio in the $FeCoNiCrMo_x$, the d-band center of VBS shifts to a higher position, and the $FeCoNiCrMo_{1.0}$ has the highest one (−2.332 eV). The $G(r)$ peaks shift to larger interatomic distances as the increase of Mo elements (2.537–2.605 Å), representing ≈2.61% tensile strain (**Figure 5**g). Generally, as tensile strain occurs, the decrease in electron orbital overlap would induce an upshift of the d-band center and narrowing of the energy band distribution, then the d electrons become more unstable, meaning that their XPS binding energies would be smaller.[31] The higher is the d-band center, the greater is the adsorption energy. These results also matched well with the above results of heat capacity. These energy traps are more widely distributed in $FeCoNiCrMo_{1.0}$, which can provide stable adsorption positions to promote catalysis. The easy adsorption of oxygen-containing species (e.g., O, OH and OOH) contributes to the oxidative formation of intermediates for liberating the active sites.[32] Hence, the addition of high-valent Mo sites accompanied by amorphization can further tune the electron structure, such as reducing the local work function, increasing the electron density, distribution, and conductivity, as well as elevating the density of states at Fermi level of $FeCoNiCrMo_x$, to promote OER activity. Correspondingly, the $FeCoNiCrMo_{1.0}$ had the smallest arc radius of the Nyquist plot related to the charge transfer resistances (R_{ct}) as shown in Figure 4g, and the resistance located in the high-frequency region reflects the ohmic resistance (R_s). Compared to that of other electrocatalysts, $FeCoNiCrMo_{1.0}$ exhibited a prominent interfacial charge transfer impedance of ≈3.1 Ω, and that of $FeCoNiCrMo_{0.6}$, $FeCoNiCrMo_{0.2}$, FeCoNiCr, and FeCoNi are 4.6, 6.1, 7.6, and 18.6 Ω, respectively, suggesting the faster charge-transfer rate and greater reaction kinetics. It is conducive to faster adsorption of reactants and conversion of intermediates. Unlike the Nyquist plots of RuO_2, the shapes of that for other samples were not simple semicircles or straight

lines, but showed a dispersion effect, suggesting the presence of a slight diffusion layer controlling on the electrode surface. The Warburg impedance of a finite diffusion layer thickness can be used to model circuits (Figure S5c, Supporting Information), which is equivalent to an RC series circuit at high frequencies. Moreover, the filling degree of the d-electrons in the band increases as the d-band center moves toward the Fermi level. It positively affects the electrical conductivity, as more carriers are available for current conduction. Additionally, the high entropy and synergistic effect of homogeneous mixing of Fe, Co, Ni, Mo, and Cr also may produce favorable local coordination environments and electronic structures that optimize the adsorption energy of the intermediates during OER reaction, thereby reducing the required overpotentials.[3b,33]

Numerous amorphous materials have emerged as a great prospect for catalysis due to structurally disordered amorphous phase that can form favorable catalytic sites.[11,34] The pair distribution function (PDF) analysis provided atomic-scale local structural information, which was conducted in Figure 5, to discover in depth the structural features of the $FeCoNiCrMo_x$ that influence their OER catalytic properties. The $G(r)$ patterns could be achieved through a fast Fourier transform of $S(Q)$.[35] Meanwhile, the average number density (ρ_0) of $FeCoNiCrMo_x$ was also obtained via $G(r)$ processed by PDFgetX2 software, which reflects changes in the atomic spacing and arrangement. $FeCoNiCrMo_{1.0}$ possessed the smallest ρ_0 (0.0925) than $FeCoNiCrMo_{0.6}$ (0.1150) and $FeCoNiCrMo_{0.2}$ (0.1230), suggesting the looser atomic arrangement. All peaks shifted right with the increase of Mo atomic ratio, indicating the volume expansion of the MRO structure. Consistent with the rise of Mo elements with large atomic sizes, the atoms stretch and become loosely arranged (Figure 5g). In addition, the ξ value, as an indicator of the correlation with amorphous ordering, is obtained via exponential function fitting of the PDF profiles.[36] $FeCoNiCrMo_{1.0}$ possessed the highest ξ value, about 5.706, as shown in Figure S11 (Supporting Information), suggesting stronger ordering that can extend to a medium-range length scale. Furthermore, the local bonding information from the PDF data was extracted to probe the coordination environments and connection modes by analyzing the Gaussian fitted curves of the first and second coordination shells for $FeCoNiCrMo_x$. Considering that the atomic radii of Fe, Co, Ni, and Cr are similar rather than that of Mo is too large, Fe-Co-Ni-Cr-Mo was characterized as pseudobinary [(Fe, Co, Ni, Cr)-Mo] with weighted partial PDFs corresponding to the (Fe, Co, Ni, Cr)- (Fe, Co, Ni, Cr), and (Fe, Co, Ni, Cr)-Mo based only on atomic size. As shown in Figure 5a–c, $T(r)$ were converted from $G(r)$ by the following equation: $[= 4\Pi r\rho(r) = G(r) + 4\Pi r\rho_0]$ to resolve the nearest-neighbor partials.[35] The relevant Gaussian fitting parameters of PDF are listed in Table S2 (Supporting Information). Some marginal distortion in Gaussian fitting is due to the compact atomic arrangement caused by the reduction of the Mo element. Nevertheless, little variation in average bond length indicated a stable SRO structure. Furthermore, the radial distribution function $g(r)$ can be obtained via the second peak of $G(r)$ with the function of $g(r) = 1 + G(r)/4\pi r\rho_0$, which reflects four kinds of correlation mode within the medium range, denoted as 1-atom (vortex-sharing), 2-atom (edge-sharing), 3-atom (face-sharing), and 4-atom (intercross-sharing) atomic cluster connections.[37] $g(r)$ has been employed to reveal the connection modes of short-range polyhedral at medium-range length scale. The unevenness of the connecting style of atomic clusters results in the splitting of the second peak of $g(r)$ in Figure 5d–f. The results showed that the 1-atom connection modes dominate in these samples (Figure 5i). However, the vortex/edge-sharing cluster connection mode transformed into the face-sharing with increased crystallinity, which is mainly reflected in the increased percentage of the 3-atom and 4-atom connection modes in $FeCoNiCrMo_{0.2}$. Figure S12 (Supporting Information) shows that $FeCoNiCrMo_{1.0}$ possessed the smallest nearest-neighbor coordination number. Generally, the fewer the atomic coordination number, the looser the surface arrangement, the narrower the band distribution, the higher the d-band center, and the stronger the adsorption energy for catalysts.[6,38] This matched Figure 4g. In short, the intimately structural interacted within short- to medium-range orders might be responsible for the outstanding OER performance of the $FeCoNiCrMo_{1.0}$.

2.3. Electron Valence Analysis

The comparative analysis of X-ray photoelectron spectroscopy (XPS) about the valence changes of the catalysts in different states (the pristine and CV-1000 cycles of $FeCoNiCrMo_{1.0}$ NPs ink) is essential to analyze the surface electrochemical states. As displayed in Figure S13 (Supporting Information), the O signal of the XPS wide-scan survey was significantly intensified after CV-1000 cycles due to the conversion of corresponding (oxy)hydroxides. According to high-resolution XPS (HR-XPS) spectra in **Figure 6**a–e, the binding energies of Cr^0, Cr^{3+}, Cr^{6+} and satellite peak were at 574.8, 576.6, 578.0, and 579.6 eV, respectively. For Mo 3d, the binding energy peaks locate at 228.2, 229.3, 231.4, and 235.6 eV are contributed by Mo^0, Mo^{4+}, Mo^{6+}, and Mo $3d_{3/2}$ peak, respectively.[39] The Ni 2p spectrum are observed that the peaks at 853.2, 856.1, 856.13, and 857.8 eV correspond to Ni^0, Ni^{2+}, Ni^{3+}, and satellite peak.[40] For Co 2p, the multi-peak spectrum can be deconvoluted to reveal a composition of Co^0, Co^{3+}, Co^{2+}, and satellite peak, with the peaks of 779.4, 781.2, 783.1, and 787.6 eV. The peaks at 707.7, 711.1, and 713.2 eV corresponded to Fe^0, Fe^{2+}, and Fe^{3+}, respectively. Especially, by comparing the positions of the XPS peaks before and after the reaction of the samples, the binding energies of the metals generated more or less positive shift in CV-1000 cycles $FeCoNiCrMo_{1.0}$. The phenomenon indicated that the metal atoms lose partial electrons, namely transfer the electrons to the oxygen atoms to form oxides. The intensity of metal zero-valence peaks is apparently reduced after the CV-1000 cycles, while that of the high valence states peaks strengthen, also indicating the generation of (oxy)hydroxide-based compounds. In other words, the reducing Fe^0, Co^0, Ni^0, Cr^0, and Mo^0 in $FeCoNiCrMo_{1.0}$ themselves are oxidized as electron donors, the downward shift of the metal d-band and overlap with the p-band of the oxygen ligand resulting in the higher valence state,[41] which enhance the covalency of M-O bonds. During the oxidation process of the metals, the potential energy increased in general and then diminished the energy barrier of the reactants on the surface of catalyst to boost electronic transfer, accelerate OER kinetics, as well as guide the reactants toward the desired product transformation.[42] Meanwhile, the lattice distortion effect of high-entropy alloys makes

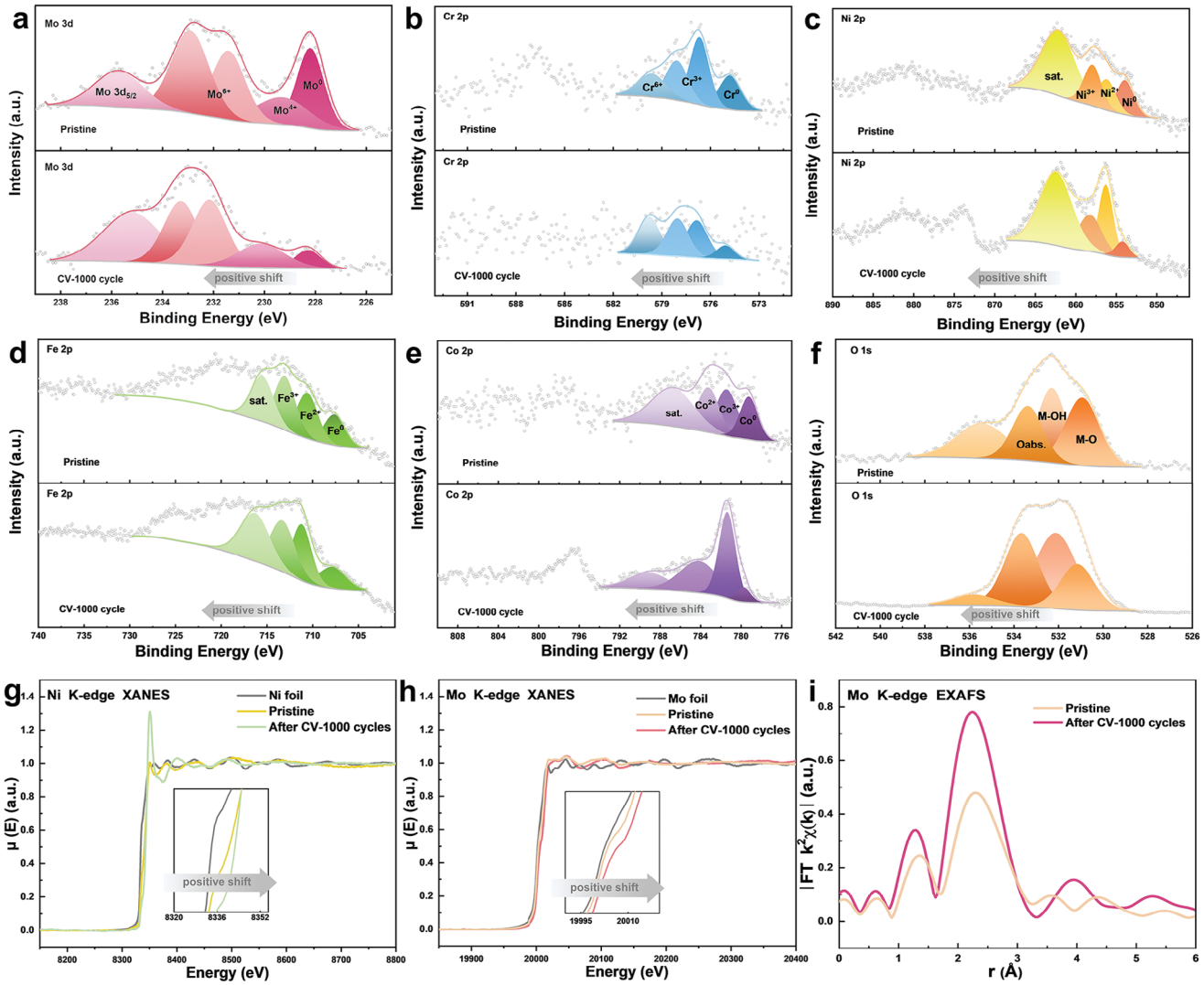

Figure 6. High-resolution XPS spectra of a) Mo 3d, b) Cr 2p, c) Ni 2p, d) Fe 2p, e) Co 2p, and f) O 1s of pristine and CV-1000 cycles $FeCoNiCrMo_{1.0}$. g) Ni K-edge, h) Mo K-edge XANES, and i) EXAFS patterns of pristine and CV-1000 cycles $FeCoNiCrMo_{1.0}$.

the atomic stacking of the system relatively loose, structurally disordered, and susceptible to surface reconstruction, OH^- can be easily incorporated into the amorphous phase to form hybrid catalyst, which synergistically improves the OER performance.

As displayed in Figure 6f. The peaks associated with the lattice oxygen bond (M—O), hydroxide bond (M—OH/M—OOH), and absorbed H_2O are located at 530.9, 532.3, and 533.3 eV. The XPS fine spectrum of O 1s can also correspond to the above results of the high valence metals generation. Furthermore, X-ray absorption spectroscopy (XAS) was performed on the pristine and CV-1000 cycles $FeCoNiCrMo_{1.0}$ to investigate the surface chemical evolution during OER process. A similar phenomenon was also seen in X-ray absorption near edge structure (XANES) of K-edge in Figure 6g,h and Figure S14 (Supporting Information). The positive shift of photoelectron to higher energy observed after CV-1000 cycling indicated the increase in the metal valence state,[43] which verified the oxidation in $FeCoNiCrMo_{1.0}$. Furthermore, the extended X-ray absorption fine structure (EXAFS) spectra of Mo K-edge intuitively demonstrated the coordination environment of Mo (Figure 6i). The peaks strengthened and shifted to a lower *R*-value after 1000 CV cycles, indicating an increased packing density around the Mo atom due to local structural rearrangements.

3. Conclusion

In summary, we have successfully synthesized $FeCoNiCrMo_{1.0}$ HEMG-NPs with high ORE activity by LE-IGC. We demonstrate that, by regulating high-valence metal Mo in $FeCoNiCrMo_x$, HEA can adjust electronic distribution and structural disorder to boost the OER performance. These findings, assisted by XPS, PDF, and EXAFS analysis, corroborated that the fewer is the atomic coordination number, the looser is the surface arrangement, the narrower is the energy band distribution, the higher is the center of the d-band, and the stronger is the adsorption energy for catalysts. As shown in Table S3 (Supporting Information), the

$FeCoNiCrMo_{1.0}$ HEMG-NPs exhibit a superior OER performance (overpotential of 243.3 mV at a current density of 10 mA cm^{-2}) to most reported catalysts and are comparable to the precious metals. The rational design of the spontaneously inhomogeneous atomic configurations for building the highly efficient electrocatalysts at the high current density represents an advancement toward further development of practical industrial water oxidation.

4. Experimental Section

Materials and Synthesis: A typical arc-melting method was used for the preparation of alloy ingots under a high-purity Ar atmosphere, and the raw metal materials of mixtures are high purity (≈99.9%). IGC, as a unique instrument for nanostructure preparation, was designed to evaporate HEA NPs from the alloy ingots via a laser beam. Then, the evaporated HEA atoms can be rapidly cooled during the collision with He gas atoms and attached to the copper roller filled with liquid nitrogen, which can be easily collected by a scraper. The fast-cooling rate makes it easier to form solid solutions, even amorphous alloys.

Characterizations: TEM, HRTEM, and EDS measurements were carried out by an JEOL JEM 2100F electron microscope. The support films on double-folding grids were used to prepare all TEM magnetic powder samples. XPS and VB-XPS data were calibrated for the C 1s peak (284.8 eV), which was recorded on an ESCALAB 250Xi spectrometer. The origin of the binding energy E_b was set to the Fermi energy E_f of the Au plate. The Shirley background is subtracted from the measured spectra. For the accurate comparison of all valence band spectra, the upper level of integration of background subtraction is fixed at 10.0 eV bonding energy position throughout all valence-band spectra. The d-band center of the valence band spectrum is given by $\int N(\varepsilon)\varepsilon d\varepsilon / \int N(\varepsilon)d\varepsilon$, where $N(\varepsilon)$ is the XPS intensity after background subtraction.[44] The work function is calculated using the tangent method according to the valence band spectrum. DSC experiments in a high-purity N_2 atmosphere were performed by Netzsch Pegasus DSC with a heating rate of 20 K min^{-1}. The hysteresis loop was measured via a physical property measurement system with the vibrating specimen magnetometer module (DYNACOOL-9, Quantum Design, USA).

HE-XRD for PDF and XAFS patterns were collected at beamline BL14B1 and BL13SSW of the Shanghai Synchrotron Radiation Facility (SSRF). Athena was used to process the X-ray absorption curves by energy shift and phase correction, normalizing and obtaining the K-space and R-space data.[45] In addition, HE-XRD in situ heating was detected at beamline 3W1 of the Beijing Synchrotron Radiation Facility (BSRF). Two-dimensional diffraction patterns were obtained by silicon detector with a data acquisition time of 1 s for each pattern. The time for data readout and storage was ≈4 s.[23] The heating rate was 20 K min^{-1}. The other spectral data were collected at room temperature in fluorescent mode. The structure factor S(Q) with $Q_{max} \approx 30$ Å^{-1} was derived from the scattering data by masking bad pixels; integrating images; subtracting the appropriate background; and correcting for oblique incidence, absorption, multiple scattering, fluorescence, Compton scattering, and Laue correction using the Fit2D and PDFgetX2 software. a Gaussian to represent a partial [$4\pi r^2 \rho_{ij}(r)$, where $\rho_{ij}(r)$ is the partial pair density function], one can express $T(r)$ as a sum of the weighted Gaussians.[46]

$$T(r) = \sum_{i} \sum_{j \le i} 4\pi r \rho_{ij}(r) W_{ij} \quad (1)$$

where i and j denote the ith and jth atomic species, and W_{ij} is the weight of the i~j pair. $W_{ij} = 2c_i c_j b_i b_j / <b>^2$ $(i \neq j)$ or $W_{ij} = c_i^2 b_i^2 / <b>^2 (i = j)$, where c_i is the atom fraction and b_i is the scattering factor of the ith element. The W_{ij} and R_{ij} of different atomic pairs are calculated based on the above equation and conducted the peak fitting of the first peak of $T(r)$. The most-probable distance (R_2) between the centers of the two connected coordination short-range clusters corresponding to 1-atom, 2-atom, 3-atom, and 4-atom can be calculated as $2R_1$, $\sqrt{3}R_1$, $\sqrt{\frac{8}{3}}R_1$, and $\sqrt{2}R_1$, where R_1 is the average bond length.[47] These are, therefore, the predicted second peak positions from the decomposed $g(r)$.

Electrochemical Measurements: Electrochemical OER measurements were assessed on an electrochemical workstation (CHI660E, Shanghai Chen Hua Ltd., China) at room temperature with the traditional three-electrode cell, and the electrolyte is 1.0 M KOH. The catalyst ink was ultrasonically dispersed in the absolute ethanol, and then dripped onto a carbon cloth, which was as the working electrode. The catalyst mass loading was ≈1.5 mg cm^{-2}. The Pt sheet and Hg/HgO electrode were used as the counter electrode and the reference electrode, respectively. All the potentials reported were referenced versus reversible hydrogen electrode (RHE). The polarization curves were conducted at a scan rate of 5 mV s^{-1} with 100% IR correction. EIS measurements were performed in the frequency range of 10^5 to 0.01 Hz at 0.6 V versus Hg/HgO for OER. Durability was evaluated by chronopotentiometry test under a constant current density of 10, 50, and 100 mA cm^{-2}. To calculate ECSA, the applied specific capacitance (20–60 µF cm^{-2}) was set as 40 µF cm^{-2}.[48] The Chronopotentiometry (CP) test or Amperometric *i*–*t* Curve (*i*–*t*) was executed to detect the stability of the catalysts.

Acknowledgements

This work was financially supported by the National Key R&D Program of China (No. 2021YFB3802800), the National Natural Science Foundation of China (Nos. 12261160364, 52222104, 22275089), and the Fundamental Research Funds for the Central Universities (No. 2024202001). This research also used resources of the Advanced Photon Source; a U.S. Depart-ment of Energy (DOE) Office of Science User Facility operated for the DOE Office of Science by Argonne National Laboratory under Contract No. DE-AC02-06CH11357. The authors thank the synchrotron experiments sup-ports of beamline BL13SSW at Shanghai Synchrotron Radiation Facility and beamline 3W1 of the Beijing Synchrotron Radiation Facility.

Conflict of Interest

The authors declare no conflict of interest.

Data Availability Statement

The data that support the findings of this study are available from the corresponding author upon reasonable request.

Keywords

high-entropy alloy, inert gas condensation, metallic glass nanoparticles, oxygen evolution reaction, synchrotron X-ray techniques

[1] F. Gu, W. Guo, Y. Yuan, Y. P. Deng, H. Jin, J. Wang, Z. Chen, S. Pan, Y. Chen, S. Wang, *Adv. Mater.* **2024**, *36*, 2313096.

[2] a) H. Li, Y. Han, H. Zhao, W. Qi, D. Zhang, Y. Yu, W. Cai, S. Li, J. Lai, B. Huang, L. Wang, *Nat. Commun.* **2020**, *11*, 5437; b) L. H. Sun, Q. Y. Li, S. N. Zhang, D. Xu, Z. H. Xue, H. Su, X. Lin, G. Y. Zhai, P. Gao, S. I. Hirano, J. S. Chen, X. H. Li, *Angew. Chem., Int. Ed.* **2021**, *60*, 25766.

[3] a) Y. Ding, Z. Wang, Z. Liang, X. Sun, Z. Sun, Y. Zhao, J. Liu, C. Wang, Z. Zeng, L. Fu, M. Zeng, L. Tang, *Adv. Mater.* **2023**, 2302860; b) J. Hu, T. Guo, X. Zhong, J. Li, Y. Mei, C. Zhang, Y. Feng, M. Sun, L. Meng, Z. Wang, B. Huang, L. Zhang, Z. Wang, *Adv. Mater.* **2024**, *36*, 2310918; c) T. Zhang, H.-F. Zhao, K.-Y. Wang, Z.-J. Chen, L. Li, J. Peng, X. Peng, Y.-J. Huang, H.-B. Yu, *Mater. Futures* **2023**, *2*, 045101; d) M. S. A. Sher Shah, G. Y. Jang, K. Zhang, J. H. J. E. Park, *EcoEnergy* **2023**, *1*, 344; e) Q. Ruan, D. Li, C. Wu, C. Huang, P. K. J. E. Chu, *EcoEnergy* **2024**, *2*, 268; f) F. Wang, P. Zou, Y. Zhang, W. Pan, Y. Li, L. Liang, C. Chen, H. Liu, S. J. N. C. Zheng, *Nat. Commun.* **2023**, *14*, 6019.

[4] P. Zhou, D. Liu, Y. Chen, M. Chen, Y. Liu, S. Chen, C. T. Kwok, Y. Tang, S. Wang, H. Pan, *J. Mater. Sci. Technol.* **2022**, *109*, 267.

[5] Q. Yuan, J. Zhao, D. H. Mok, Z. Zheng, Y. Ye, C. Liang, L. Zhou, S. Back, K. Jiang, *Nano Lett.* **2021**, *22*, 1257.

[6] Z. W. Seh, J. Kibsgaard, C. F. Dickens, I. Chorkendorff, J. K. Nørskov, T. F. Jaramillo, *Science* **2017**, 355.

[7] a) D. Zhang, H. Zhao, X. Wu, Y. Deng, Z. Wang, Y. Han, H. Li, Y. Shi, X. Chen, S. Li, J. Lai, B. Huang, L. Wang, *Adv. Funct. Mater.* **2021**, *31*, 2006939; b) H. Li, J. Lai, Z. Li, L. Wang, *Adv. Funct. Mater.* **2021**, *31*, 2106715.

[8] M. W. Glasscott, A. D. Pendergast, S. Goines, A. R. Bishop, A. T. Hoang, C. Renault, J. E. Dick, *Nat. Commun.* **2019**, *10*, 2650.

[9] B. Song, Y. Yang, M. Rabbani, T. T. Yang, K. He, X. Hu, Y. Yuan, P. Ghildiyal, V. P. Dravid, M. R. Zachariah, W. A. Saidi, Y. Liu, R. Shahbazian-Yassar, *ACS Nano* **2020**, *14*, 15131.

[10] H. Li, J. Lai, Z. Li, L. Wang, *Adv. Funct. Mater.* **2021**, *31*, 2106715.

[11] M. Yan, S. Chen, S. Wu, X. Zhou, S. Fu, D. Wang, C. Kübel, H. Hahn, S. Lan, T. Feng, *J. Mater. Sci. Technol.* **2024**, *170*, 212.

[12] M. Wei, Y. Sun, J. Zhang, F. Ai, S. Xi, J. Wang, *Energy Environ. Sci.* **2023**, *16*, 4009.

[13] J. K. Nørskov, F. Abild-Pedersen, F. Studt, T. Bligaard, *Proc. Natl. Acad. Sci. U. S. A.* **2011**, *108*, 937.

[14] L. Yi, S. Xiao, Y. Wei, D. Li, R. Wang, S. Guo, W. Hu, *Chem. Eng. J.* **2023**, 469.

[15] X. Bo, Y. Li, X. Chen, C. Zhao, *Chem. Mater.* **2020**, *32*, 4303.

[16] F. Wang, A. Inoue, F. L. Kong, Y. Han, S. L. Zhu, E. Shalaan, F. Al-Marouki, *J. Alloys Compd.* **2018**, *732*, 637.

[17] H. He, B. Wang, S. Lan, J. P. C. Ruff, C. Sun, M. Naeem, C.-T. Liu, X.-L. Wang, *J. Osteopath. Med.* **2021**, *73*, 3285.

[18] X. Zhou, L. Zou, H. Zhu, M. Yan, J. Wang, S. Lan, S. Chen, H. Hahn, T. Feng, *Small* **2023**, 2310327.

[19] T. Löffler, A. Ludwig, J. Rossmeisl, W. Schuhmann, *Angew. Chem., Int. Ed.* **2021**, *60*, 26894.

[20] P. Yang, Z. Jiang, Y. Shi, W. Zhang, X. Ren, L. Liang, M. Wang, K. Zhu, *Appl. Phys. Lett.* **2023**, 123.

[21] J. Wang, S. Wu, S. Fu, S. Liu, Z. Ren, M. Yan, S. Chen, S. Lan, H. Hahn, T. Feng, *J. Mater. Sci. Technol.* **2021**, *77*, 126.

[22] Y. H. Meng, S. Y. Zhang, W. H. Zhou, J. H. Yao, S. N. Liu, S. Lan, Y. Li, *Acta Mater.* **2022**, 241.

[23] J. Ge, Y. Gu, Z. Yao, S. Liu, H. Ying, C. Lu, Z. Wu, Y. Ren, J.-i. Suzuki, Z. Xie, Y. Ke, J. Zeng, H. Zhu, S. Tang, X.-L. Wang, S. Lan, *J. Mater. Sci. Technol.* **2024**, *176*, 224.

[24] H. Luan, X. Zhang, H. Ding, F. Zhang, J. H. Luan, Z. B. Jiao, Y.-C. Yang, H. Bu, R. Wang, J. Gu, C. Shao, Q. Yu, Y. Shao, Q. Zeng, N. Chen, C. T. Liu, K.-F. Yao, *Nat. Commun.* **2022**, 13.

[25] Q. F. He, P. H. Tang, H. A. Chen, S. Lan, J. G. Wang, J. H. Luan, M. Du, Y. Liu, C. T. Liu, C. W. Pao, Y. Yang, *Acta Mater.* **2021**, *216*, 117140.

[26] C. Pei, S. Chen, T. Zhao, M. Li, Z. Cui, B. Sun, S. Hu, S. Lan, H. Hahn, T. Feng, *Adv. Mater.* **2022**, 34.

[27] a) Y. Hou, Z. Qin, X. Han, Y. Liu, W. Zhang, X. Cao, Y. Cao, J.-P. Lang, H. Gu, *Nanoscale* **2024**, *16*, 6662; b) Y. Zhu, M. Klingenhof, C. Gao, T. Koketsu, G. Weiser, Y. Pi, S. Liu, L. Sui, J. Hou, J. Li, H. Jiang, L. Xu, W.-H. Huang, C.-W. Pao, M. Yang, Z. Hu, P. Strasser, J. Ma, *Nat. Commun.* **2024**, *15*, 1447.

[28] S.-Q. Chang, C.-C. Cheng, P.-Y. Cheng, C.-L. Huang, S.-Y. Lu, *Chem. Eng. J.* **2022**, *446*, 137452.

[29] T. X. Nguyen, Y. H. Su, C. C. Lin, J. Ruan, J. M. Ting, *Adv. Sci.* **2021**, *8*, 2002446.

[30] X. Duan, J. Kang, W. Tian, H. Zhang, S.-H. Ho, Y.-A. Zhu, Z. Ao, H. Sun, S. Wang, *Appl. Catal., B* **2019**, *256*, 117795.

[31] D. Liu, Q. Zeng, C. Hu, D. Chen, H. Liu, Y. Han, L. Xu, Q. Zhang, J. Yang, *Nano Res. Energy* **2022**, *1*, e9120017.

[32] T. A. A. Batchelor, J. K. Pedersen, S. H. Winther, I. E. Castelli, K. W. Jacobsen, J. Rossmeisl, *Joule* **2019**, *3*, 834.

[33] Y. Mei, Y. Feng, C. Zhang, Y. Zhang, Q. Qi, J. J. A. C. Hu, **2022**, *12*, 10808.

[34] a) J. Li, G. Doubek, L. McMillon-Brown, A. D. Taylor, **2019**, *31*, 1802120; b) Q. Wang, J. Li, Y. Li, G. Shao, Z. Jia, B. Shen, *Nano Res.* **2022**, *15*, 8751.

[35] S. Fu, G. X. Chen, H. Guo, S. Liu, M. Yan, Y. Lou, H. Ying, Z. Yao, Y. Ren, W. Jiang, H. Zhu, H. Hahn, T. Feng, S. Lan, *Small* **2023**, *19*, 2370257.

[36] Y. Lou, Z. Yao, S. Fu, S. Liu, X. Zhu, W. Huang, M. Dong, J. Zeng, H. Lin, H. Zhu, S. Lan, *Prog. Nat. Sci.: Mater. Int.* **2023**, *33*, 244.

[37] F.-Y. Gao, S.-N. Liu, J.-C. Ge, X.-L. Zhang, L. Zhu, Y.-R. Zheng, Y. Duan, S. Qin, W. Dong, X. Yu, R.-C. Bao, P.-P. Yang, Z.-Z. Niu, Z.-G. Ding, W. Liu, S. Lan, M.-R. Gao, Y. Yan, S.-H. Yu, *Nat. Catal.* **2022**, *5*, 993.

[38] L. A. Kibler, A. M. El-Aziz, R. Hoyer, D. M. Kolb, *Angew. Chem., Int. Ed.* **2005**, *44*, 2080.

[39] S. Ramakrishnan, J. Balamurugan, M. Vinothkannan, A. R. Kim, S. Sengodan, D. J. Yoo, *Appl. Catal., B* **2020**, *279*, 119381.

[40] Z. Jia, T. Yang, L. Sun, Y. Zhao, W. Li, J. Luan, F. Lyu, L. C. Zhang, J. J. Kruzic, J. J. Kai, J. C. Huang, J. Lu, C. T. Liu, *Adv. Mater.* **2020**, *32*, 2000385.

[41] R. K. Patel, R. N. Jenjeti, R. Kumar, N. Bhattacharya, S. Kumar, S. K. Ojha, Z. Zhang, H. Zhou, K. Qu, Z. Wang, Z. Yang, C. Klewe, P. Shafer, S. Sampath, S. Middey, *Appl. Phys. Rev.* **2023**, 10.

[42] Z. J. Chen, T. Zhang, X. Y. Gao, Y. J. Huang, X. H. Qin, Y. F. Wang, K. Zhao, X. Peng, C. Zhang, L. Liu, M. H. Zeng, H. B. Yu, *Adv. Mater.* **2021**, *33*, 2101845.

[43] P. F. Liu, S. Yang, L. R. Zheng, B. Zhang, H. G. Yang, *Chem. Sci.* **2017**, *8*, 3484.

[44] a) X. Wang, S. Li, Z. Yuan, Y. Sun, Z. Tang, X. Gao, H. Zhang, J. Li, S. Wang, D. Yang, J. Xie, Z. Yang, Y. M. Yan, *Angew. Chem., Int. Ed.* **2023**, *62*, e202303794; b) X. Wu, F. Chen, N. Zhang, Y. Lei, Y. Jin, A. Qaseem, R. L. Johnston, *Small* **2017**, *13*, 1603387; c) W. P. Zhou, A. Lewera, R. Larsen, R. L. Masel, P. S. Bagus, A. Wieckowski, *J. Phys. Chem. B 110*, 13393; d) V. R. Stamenkovic, B. Fowler, B. S. Mun, G. F. Wang, P. N. Ross, C. A. Lucas, N. M. Markovic, *Science* **2007**, *315*, 493.

[45] Z. P. Wu, H. Zhang, S. Zuo, Y. Wang, S. L. Zhang, J. Zhang, S. Q. Zang, X. W. Lou, *Adv. Mater.* **2021**, *33*, 2103004.

[46] D. Ma, A. D. Stoica, L. Yang, X. L. Wang, Z. P. Lu, J. Neuefeind, M. J. Kramer, J. W. Richardson, T. Proffen, *Appl. Phys. Lett.* **2007**, 90.

[47] J. Ding, E. Ma, M. Asta, R. O. Ritchie, *Sci. Rep.* **2015**, *5*, 17429.

[48] N. Zhang, X. Feng, D. Rao, X. Deng, L. Cai, B. Qiu, R. Long, Y. Xiong, Y. Lu, Y. Chai, *Nat. Commun.* **2020**, *11*, 4066.